Wind and Structures, *Vol. 22, No. 1 (2016) 17-41*
DOI: http://dx.doi.org/10.12989/was.2016.22.1.017

Numerical simulation of 3-D probabilistic trajectory of plate-type wind-borne debris

Peng Huang[a], Feng Wang[b], Anmin Fu and Ming Gu[*]

State Key Laboratory of Disaster Reduction in Civil Engineering, Tongji University, Shanghai 200092, China

(Received March 16, 2014, Revised May 20, 2015, Accepted June 27, 2015)

Abstract. To address the uncertainty of the flight trajectories caused by the turbulence and gustiness of the wind field over the roof and in the wake of a building, a 3-D probabilistic trajectory model of flat-type wind-borne debris is developed in this study. The core of this methodology is a 6 degree-of-freedom deterministic model, derived from the governing equations of motion of the debris, and a Monte Carlo simulation engine used to account for the uncertainty resulting from vertical and lateral gust wind velocity components. The influence of several parameters, including initial wind speed, time step, gust sampling frequency, number of Monte Carlo simulations, and the extreme gust factor, on the accuracy of the proposed model is examined. For the purpose of validation and calibration, the simulated results from the 3-D probabilistic trajectory model are compared against the available wind tunnel test data. Results show that the maximum relative error between the simulated and wind tunnel test results of the average longitudinal position is about 20%, implying that the probabilistic model provides a reliable and effective means to predict the 3-D flight of the plate-type wind-borne debris.

Keywords: probabilistic trajectory model; plate-type wind-borne debris; turbulent wind field; random gust; Monte-Carlo simulation

1. Introduction

Extreme wind events, such as hurricanes, typhoons, tornadoes, and tropical storms, pose a threat to residential structures, commercial buildings and public infrastructure all around the world. Previous studies (Kareem 1986, Lee 1988, Minor 1994) have revealed that debris created by strong wind is a major source of damage to building environment. More specifically, flying windborne debris can penetrate the building envelope system, and consequently result in the internal pressurization leading to subsequent structural damage. As a consequence of missile impact, the failure of the building envelope also allows wind-driven rain to intrude building interiors causing subsequent damage to building contents. Moreover, the possibility of flying debris inside the building and the generation of new debris likely endanger the safety of occupants.

According to the NAHB Research Center (2002), plate-type wind-borne debris is the main type of debris which causes the damage of building envelopes in the three types of wind-borne debris

*Corresponding author, Professor, E-mail: minggu@tongji.edu.cn
[a] Ph.D., E-mail: huangtju@tongji.edu.cn
[b] Ph.D. Student, E-mail: 13wafer@tongji.edu.cn

http://www.techno-press.org/?journal=was&subpage=8 ISSN: 1226-6116 (Print), 1598-6225 (Online)

classified by Wills *et al.* (2002). Sheet type debris has been investigated by a number of researchers (Richards *et al.* 2008, Noda and Nagao 2010, Fu *et al*. 2013). However, they mainly focused on the flight characteristics of the debris or the debris in a specific condition, and do not include the interaction of debris and wind field. In fact, the wake flow of the building and wind field over the roof significantly affects the flight trajectories of the debris. More recently, Visscher and Kopp (2007), Kordi *et al.* (2010), and Kordi and Kopp (2011) examined the flight of the plate-type debris by conducting wind tunnel testing, and discussed the effects of aerodynamic characteristics, wake flow and wind field of the building on the flight trajectory of the debris. They observed that the flight characteristics of the debris in actual turbulent flow field were uncertain. Grayson *et al.* (2012) established a 6-degree-of-freedom (DoF) probabilistic trajectory model of plate-type debris to simulate the uncertainty of the flight trajectory, including the wind turbulence and variation of wind direction. However, the probabilistic trajectory model has low computational efficiency and accuracy as it utilized Euler angles to describe the 3-D rotation of the plate-type wind-borne debris. Moreover, the uncertainty of wind speed was not accounted for and the validity of their deterministic model has not been established. Therefore, it is necessary to develop a more accurate model to simulate the flight trajectories of the wind-borne debris in a turbulent wind field.

This study presents a probabilistic approach to estimate the trajectory of the plate-type debris for a given initial condition. The basis of this methodology is a deterministic flight trajectory model in the steady-state wind flow, in which the quaternions are used to describe the 3-D rotation of the plate-type wind-borne debris to free it from the gimbal lock (Fu *et al*. 2013). This proposed methodology also addresses the uncertainty in the estimation of debris trajectory in turbulent flow by taking into account vertical and lateral velocity components generated by a Monte Carlo simulation engine. The accuracy of the probabilistic model was calibrated and validated (Roache 1997) via the comparison of the simulated data to the wind tunnel data in Kordi *et al*. (2010). This framework can be used to build the catastrophe risk model and analyze the vulnerability of structures to strong winds.

2. Methodology

2.1 Rigid body motion and the definition of coordinate systems

The classical Newton-Euler equations describes the combined translation and rotation dynamics of a rigid body, using a rotating reference frame with its axes fixed to the body and parallel to the body's principal axes of inertia

$$m\frac{d\mathbf{V}_g}{dt} = \mathbf{F}_g \tag{1}$$

$$\mathbf{I}_p\frac{d\boldsymbol{\omega}_p}{dt} = \mathbf{M}_P - \boldsymbol{\omega}_p \times \mathbf{I}_p\boldsymbol{\omega}_p \tag{2}$$

where the subscript *g* represents that a quantity is expressed in the global inertial reference frame and subscript *p* indicates that a quantity is expressed in the body-fixed coordinate. Generally, translational motion of a plate is described in the global inertial reference frame while its rotational motion is defined in the body-fixed coordinate. The translating reference frame is used to connect these two coordinates, and its axes X_t, Y_t, Z_t are parallel to the global inertial axes but move

with the object. Further, the body-fixed axes of the body X_p, Y_p, Z_p are defined by the Euler angles ϕ, θ, ψ as illustrated in Fig. 1. From translating reference frame X_t, Y_t, Z_t to body-fixed reference frame X_p, Y_p, Z_p, the translating reference frame X_t, Y_t, Z_t first need rotate a ψ degree with Z_t axis and the reference frame X_1, Y_1, Z_t is derived. Then, the reference frame X_1, Y_1, Z_t need rotate a θ degree with Y_1 axis and the reference frame X_p, Y_1, Z_1 is derived. At last, the reference frame X_p, Y_1, Z_1 need rotate a ϕ degree with X_p axis and the rotating body-fixed reference frame X_p, Y_p, Z_p is derived. Fig. 1 shows the three different coordinate systems, in which *x*-axis stands for the longitudinal direction, *y*-axis stands for the vertical direction, and *z*-axis stands for the lateral direction.

In the results that follow, the trajectory of windborne debris is presented in the global coordinate system. A transformation matrix is introduced in order to implement the conversion between global inertial reference frame and body-fixed reference frame. Fu *et al*. (2013) illustrated the disadvantage of Euler angles method (Grayson *et al*. 2012) to describe the 3-D rotation of rigid body. There exist singularities when the parameters of Euler angles are utilized into numerical integration, and this would lead to the gimbal lock and the reduction of computational efficiency. The rotational quaternions of the 3-D rotation of rigid body are

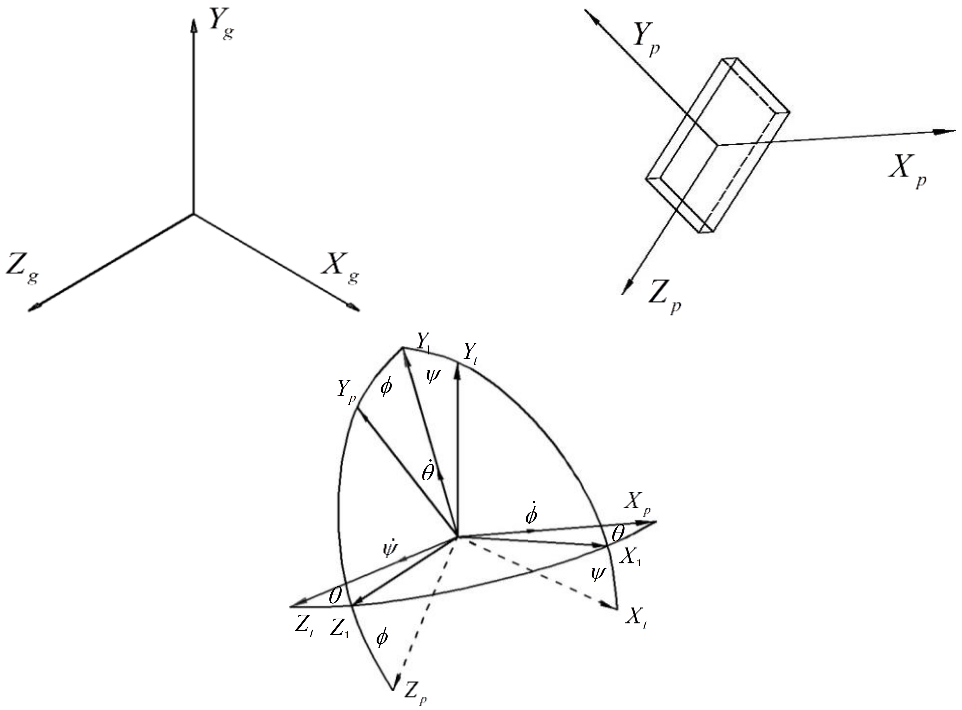

Fig. 1 Illustration of the global inertial reference frame, X_g, Y_g, Z_g, the rotating body-fixed reference frame, X_p, Y_p, Z_p, the relationship between translating reference frame, X_t, Y_t, Z_t, and the rotating body-fixed reference frame, X_p, Y_p, Z_p, defined with Euler angles, ϕ, θ, ψ

$$\mathbf{q} = \begin{bmatrix} q_0 \\ q_1 \\ q_2 \\ q_3 \end{bmatrix} = \begin{bmatrix} \cos(\phi/2) \\ p_1 \sin(\phi/2) \\ p_2 \sin(\phi/2) \\ p_3 \sin(\phi/2) \end{bmatrix} \tag{3}$$

Rotational quaternion represents a rotation ϕ about an axis $\mathbf{p}$, and p_1, p_2, p_3 are the components of the unit vector $\mathbf{p}$ in reference frame. In addition, in order for a quaternion to represent a pure rotation, it is constrained to be a unit quaternion, having a unit norm, $\|\mathbf{q}\|$.

$$\|\mathbf{q}\| = \sqrt{\mathbf{q}^T \cdot \bar{\mathbf{q}}} = \sqrt{q_0^2 + q_1^2 + q_2^2 + q_3^2} = 1 \tag{4}$$

Eq. (4) must be enforced to prevent any scaling of transformed coordinates, where $\bar{\mathbf{q}} = [q_0, -q_1, -q_2, -q_3]^T$ is the adjoint of the quaternion.

Given a vector $\mathbf{x}_t$ in the translating reference frame, then $\mathbf{x}_p$, its representation in the body-fixed reference frame, can be obtained using rotational quaternions

$$\begin{bmatrix} 0 \\ \mathbf{x}_p \end{bmatrix} = \mathbf{q} \cdot \begin{bmatrix} 0 \\ \mathbf{x}_t \end{bmatrix} \cdot \bar{\mathbf{q}} = \begin{bmatrix} 1 & \mathbf{0}^T \\ \mathbf{0} & R_q(\mathbf{q}) \end{bmatrix} \begin{bmatrix} 0 \\ \mathbf{x}_t \end{bmatrix} \tag{5}$$

where $R_q(\mathbf{q})$ is a quaternion based rotational matrix

$$R_q(\mathbf{q}) = \begin{pmatrix} q_0^2 + q_1^2 - q_2^2 - q_3^2 & 2q_1q_2 + 2q_0q_3 & 2q_1q_3 - 2q_0q_2 \\ 2q_1q_2 - 2q_0q_3 & q_0^2 - q_1^2 + q_2^2 - q_3^2 & 2q_2q_3 + 2q_0q_1 \\ 2q_1q_3 + 2q_0q_2 & 2q_2q_3 - 2q_0q_1 & q_0^2 - q_1^2 - q_2^2 + q_3^2 \end{pmatrix} \tag{6}$$

In addition, it is necessary to determine the relationship between the vector of quaternion rates, $\dot{\mathbf{q}}$, and the angular velocity vector $\boldsymbol{\omega}_p$ in the body-fixed coordinates. It can be obtained using the inverse conjugate quaternion rates matrix, $[W^{'}(\mathbf{q})]^T$, as

$$\dot{\mathbf{q}} = \frac{1}{2}[W^{'}(\mathbf{q})]^T \boldsymbol{\omega}_p \tag{7}$$

$$[W^{'}(\mathbf{q})]^T = \begin{bmatrix} -q_1 & -q_2 & -q_3 \\ q_0 & -q_3 & q_2 \\ q_3 & q_0 & -q_1 \\ -q_2 & q_1 & q_0 \end{bmatrix} \tag{8}$$

Unlike the Euler angle rates matrix, the quaternion rates matrix is valid for all possible orientations in 3-D space. In addition, quaternion is much more accurate and efficient than Euler angle, especially when used to integrate incremental changes in orientation over time. The post-correction approach presented in the studies of Cline and Pai (2003) is used to correct the normality constraint error at each time-step.

2.2 Deterministic trajectory model

The 6-DoF plate debris trajectory model in this study utilizes the quaternion to describe

three-dimensional rotation in 3-D space. Assume a plate is travelling with velocity $\mathbf{V}=[V_x,V_y,V_z]^T$ in global inertial reference frame at a uniform, horizontal wind field which has a velocity vector of $\mathbf{U}=[U_x,0,0]^T$. The relative velocity of the plate to the air is $\mathbf{U}_t=\mathbf{V}-\mathbf{U}$. In order to calculate the flow angles of the debris (i.e., angle of attack and tilt angle), the relative velocity in translating reference frame, $\mathbf{U}_t$, must be transformed into the body-fixed reference frame, $\mathbf{U}_p$, using Eq. (5). Once $\mathbf{U}_p$ is obtained, the angle of attack, ε, and the tilt angle, γ, can be calculated, as illustrated in Fig. 2.

It has been well known that the force coefficients, $\mathbf{C}_F$, is a function of the angle of attack, ε, the tilt angle, γ, and the plate geometry, G. The force coefficients used in this study are chosen from Richards (2010) and substituted into the calculation of the force acting on the plate in plate-fixed reference frame afterward

$$\mathbf{F}_P=\mathbf{C}_F(\varepsilon,\gamma,G)\frac{1}{2}\rho_a\left|\mathbf{U}_p\right|^2 A_r=\begin{pmatrix}F_{PX}\\F_{PY}\\F_{PZ}\end{pmatrix}=\frac{1}{2}\rho_a\left|\mathbf{U}_p\right|^2\begin{pmatrix}C_{FX}(\varepsilon,\gamma,G)l_Y l_Z\\C_{FY}(\varepsilon,\gamma,G)l_X l_Z\\C_{FZ}(\varepsilon,\gamma,G)l_X l_Y\end{pmatrix} \tag{9}$$

where l_X, l_Y, l_Z represents the dimensions of the rigid body at X, Y, Z axis, respectively. Richards (2010) states that the only significant force is the normal force F_{PX} for plate, and the reference area of the plate A_r, is the area perpendicular to the plate-fixed axis of interest. Similar to the significant effect of Magnus force on two-dimensional trajectories of plates (Holmes 2006), the 3-D rotation of plates will result in the change in normal force coefficient (Richards 2008)

$$\Delta C_N=\text{sign}\left(\frac{d\varepsilon}{dt}\cdot\cos(\varepsilon)\right)\cdot\frac{2\pi}{1+2/AR}\min\left(\left|\frac{d\varepsilon}{dt}\frac{c\cos(\varepsilon)}{2\left|\mathbf{U}_P\right|}\right|,0.4\right) \tag{10}$$

$$AR=\frac{b^2}{A}=\frac{\left(l_Z\times\left|\cos(\gamma)\right|+l_Y\times\left|\sin(\gamma)\right|\right)^2}{A} \tag{11}$$

The moments applied to the plate are given by

$$\mathbf{M}_p=\mathbf{M}_E+\mathbf{M}_D \tag{12}$$

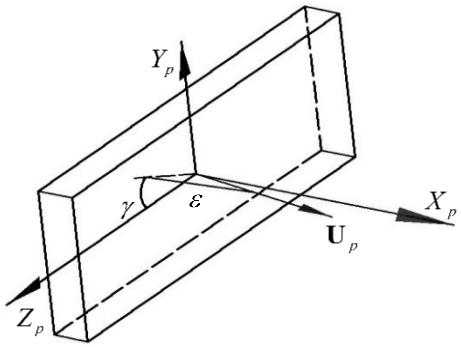

Fig. 2 Definition of the flow angles in body-fixed reference frame

where $\mathbf{M}_p$ is the total moment vector in the plate-fixed reference frame; and $\mathbf{M}_E$ is the external applied moment vector, which can be determined in accordance with the methodology in Richards (2008). Without some forms of damping, the plates would continue to rotate without bound (Richard 2008). This requires the addition of the damping moment vector, $\mathbf{M}_D$, defined as follows

$$\mathbf{M}_D = \mathbf{C}_{DM} \frac{1}{2} \rho (|\mathbf{U}_P| + |\boldsymbol{\omega}_p| l/2) A_r l^2 \boldsymbol{\omega}_p \tag{13}$$

where $\mathbf{C}_{DM}$ is the damping moment coefficient vector defined by Richards (2008)

$$\mathbf{C}_{DM} = [C_{DMX}, C_{DMY}, C_{DMZ}]^T = [-0.01, -0.185, -0.2]^T \tag{14}$$

The database of normal force coefficient $C_{FX}(\varepsilon, \gamma, G)$ used in Eq. (9) is obtained from wind tunnel tests performed at the University of Auckland (Richards 2010), in which the attack angle and tilt angle were incremented in specific intervals between 0° and 90°. In order to transfer the data to trajectory program, a linear interpolation is performed between measured values.

The force $\mathbf{F}_P$ in plate-fixed reference frame needs to be transformed back to the global inertial reference frame and used in the translational motion of plate debris

$$m \frac{d\mathbf{V}_g}{dt} = \mathbf{F}_t - mg\mathbf{j} \tag{15}$$

The rotational motion of plate debris is calculated in plate-fixed reference frame using Eqs. (2) and (7). Due to the coupling that is present in the equation of motion, Eqs. (2), (7) and (13) are solved numerically by Runge-Kutta method. These solutions are then utilized for the solutions of the next time step, the process is repeated until the plate impacts the ground.

2.3 Probabilistic trajectory model

To account for the uncertainty of the flight trajectories of wind-borne debris due to the wind field over the roof, wake flow, and gust wind, the random vertical $U_y = \delta_v U_x$ and lateral $U_z = \delta_w U_x$ gust speed components are introduced. The initial velocity vector is expressed as follows

$$\mathbf{U} = [U_x, \delta_v U_x, \delta_w U_x]^T \tag{16}$$

where U_x is denoted as the longitudinal wind velocity; and the vertical gust factor (δ_v) and lateral gust factor (δ_w) are assumed to be uniformed distributed

$$\delta_v \sim U(-\delta_{v\max}, \delta_{v\max}) \tag{17}$$

$$\delta_w \sim U(-\delta_{w\max}, \delta_{w\max}) \tag{18}$$

The bounds for the gust factor uniform distribution are determined by comparing the simulation results against the wind tunnel test data in Kordi *et al*. (2010). The introduction of gust winds enables the wind speed and wind direction to be random during the flight of the debris since the gust factor is updated at each time interval. The flight trajectories, even with the same initial

conditions, are then different for every instance of the debris' flight. Thus, some aspects of the turbulence in the wind are captured using this approach.

3. Parametric study

3.1 Initial wind speed

The wind tunnel test data in Kordi *et al*. (2010) served as the benchmark for the simulated results obtained using the probabilistic trajectory model. A 1:20 scale low-rise building model was tested in the wind tunnel. The prototype of the model is 9.14 m wide by 10.38 m long, with an eave height of 6 m. The gable roof has a pitch of 1:3, and the roof sheathing has dimensions of 1.2 m by 2.4 m with a thickness of 12.7 mm. The roof sheathing of the low-rise building and the wind direction are shown in Fig. 3, and the initial positions of a specific roof panel at various wind directions are shown in Table 1.

Table 1 Initial conditions of the roof sheathing used for analysis

Wind speed (U)				Initial position			Initial orientation		
Mean	Std.	Gumbel Distribution		X_0	Y_0	Z_0	ϕ	θ	ψ
(m/s)	(m/s)	μ	α	(m)	(m)	(m)	(°)	(°)	(°)
56	2.2	55.01	0.58	0.60	7.56	3.70	0	0	71.6
45	1.4	44.37	0.92	−0.38	7.56	3.73	0	−15	71.6
41	1.6	40.28	0.80	−0.33	7.56	3.50	0	−30	71.6
40	1.5	39.32	0.86	−2.19	7.56	3.04	0	−45	71.6
38	1.4	37.37	0.92	−2.90	7.56	2.37	0	−60	71.6

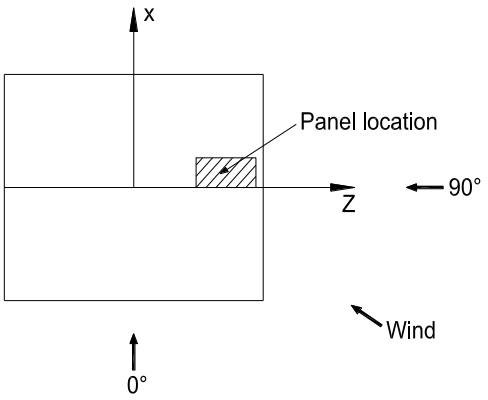

Fig. 3 Location of the roof sheathing and the definition of the wind direction

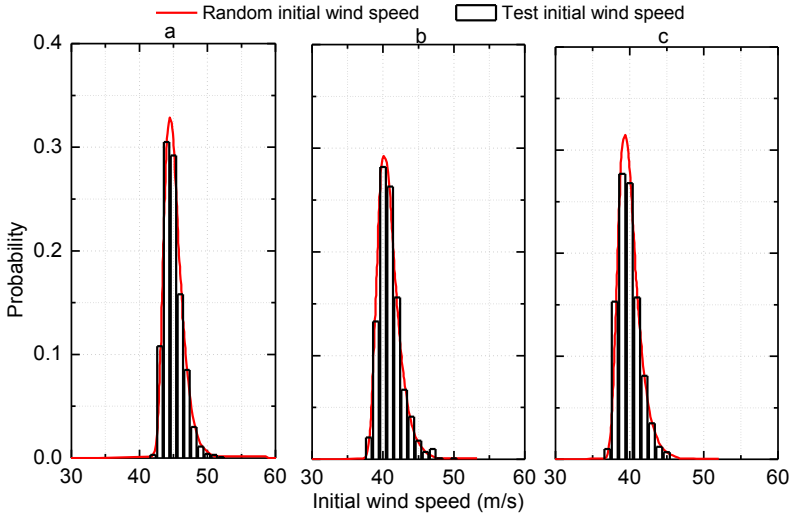

Fig. 4 Initial wind speed probabilistic models in wind direction of (a) 15°, (b) 30° and (c) 45°

Kordi *et al*. (2010) converted the roof sheathing failure speed in the wind tunnel to 3 s gust wind speed at the mean roof height, which was found to follow the Gumbel distribution, as shown in Table 1. Moreover, it is assumed that the initial wind speed is the same as equivalent 3 s gust wind speed and it is the mean wind speed during the flight of the roof sheathing. The assumption of the mean wind speed is reasonable as the flight time of the debris tend to be a few seconds (Lin *et al*. 2006).

The Gumbel Distribution is shown as

$$F(x) = \exp\{-\exp[-\alpha(x-u)]\} \tag{19}$$

$$\alpha = \frac{1.28255}{\sigma}, u = \mu - \frac{0.57722}{\alpha} \tag{20}$$

where u is a location parameter, α is a scale factor, μ and σ are the mean and standard deviation of the wind initial speed, respectively. The parameters of u and α in Gumbel Distribution are obtained from the mean and standard deviation of initial wind speed, and are shown in Table 1. The inverse function method is utilized to generate the random initial wind speed (Warga 1976). Fig. 4 show that the random generated initial wind speeds agree well with the test wind speed in the wind direction of 15°, 30° and 45°.

3.2 Time step

In order to provide a reasonable assessment of the actual solution to Eqs. (1) and (2), small time step increments are desirable for the assurance of the accuracy of the classical Runge-Kutta. However, a probabilistic trajectory model utilized to assess building envelope failures must be simulated thousands of times to ensure that the simulation is a reasonable assessment of the physical situation. This leads to increased time duration for simulation. Accordingly, there is a

trade-off between the computation intensity and prediction accuracy. In order to address this issue, the sensitivity analysis on the time interval necessary for analysis was performed.

Six parameters (i.e., debris flight time, longitudinal position, lateral position, longitudinal velocity, vertical velocity, lateral velocity) were tested at different time intervals (0.005 s, 0.01 s, 0.015 s,…, 0.1 s) with a reference time step of 0.003 s. The relative error is defined as

$$\varepsilon = \frac{x - x_0}{x_0} \tag{21}$$

where x is the value of the parameter of interest and x_0 is the value of the parameters at the reference time step.

Fig. 5 illustrates the variation of the relative error of the flight parameters with the time interval used for analysis. In these simulations, the initial conditions are deterministic and the relative errors are produced from single runs. Generally, as the time step increase, the relative error of each flight parameter in the longitudinal and vertical direction rise. However, this is not the case for the lateral position and lateral velocity. That is because the value of lateral position and lateral velocity are small compared with other flight parameters. In the wind direction of 0°, 30° and 45°, the relative errors of debris flight time and debris impacted position are lower than that of in the wind direction of 15° and 60°. However, for the impacted velocity of the debris, there has a higher accuracy in the wind direction of 0°, 15° and 30° than that of in the wind direction of 45° and 60°.

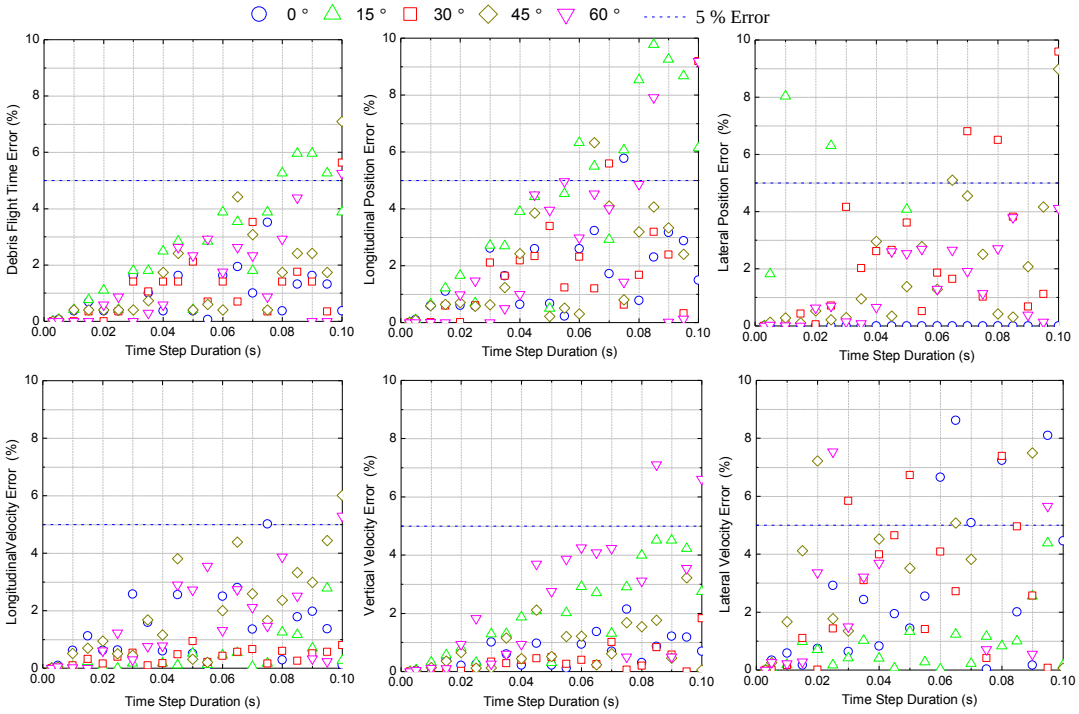

Fig. 5 Sensitivity of the flight parameters to the duration of the time step at a reference time step of 0.003 s

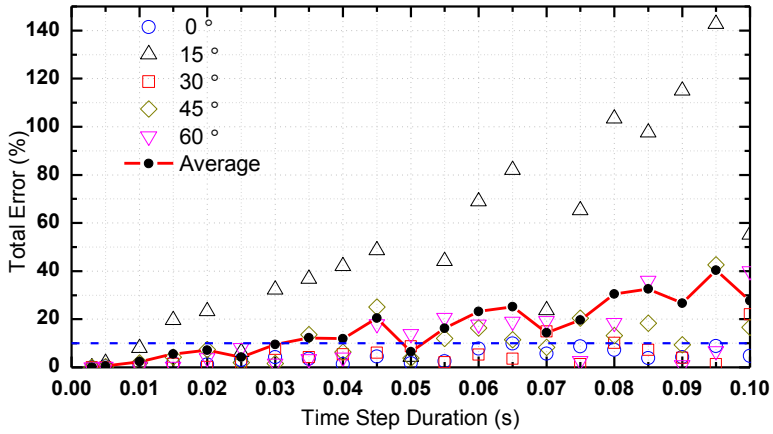

Fig. 6 Total error and average total error of the flight parameters varying with time steps for all wind directions

Fig. 6 depicts the square root of the sum of the squares (SRSS) error $\varepsilon_{\text{total}}$ for each wind direction obtained from the individual parameter error in Fig. 5 and the expected total error of all wind directions. The total error is given by

$$\varepsilon_{\text{total}} = \sqrt{\varepsilon_t^2 + \varepsilon_x^2 + \varepsilon_z^2 + \varepsilon_u^2 + \varepsilon_v^2 + \varepsilon_w^2} \tag{22}$$

where ε_t is the relative error for the debris flight time, ε_x and ε_z are the relative error for the debris landing position, and ε_u, ε_v and ε_w are the relative error for the debris landing velocity. In general, the total error of the flight parameters grows with the increase of the time step. While the total error of the flight parameters for each time step under the wind direction of 15° is far greater than that of under the wind direction of 0°, 30°, 45° and 60°. That's because the flight mode of the debris under the wind direction of 15° is more complex than that of other wind direction (Kordi *et al.* 2010). According to the wind tunnel test of Kordi *et al.* (2010), the flight modes of the debris in the wind direction of 15° can be auto-rotational, 3D spinning and translational. However, the flight modes of 0° are just auto-rotational and translational, and the flight modes for other 3 wind directions (30°~60°) are only 3D spinning. Therefore, the time step should be small enough to ensure the accuracy of the simulation. Results show that the average total error at 0.05 s is less than 10%, and consequently it is appropriate to take 0.05s as the time interval for the probabilistic debris trajectory model.

3.3 Gust sampling frequency

The random vertical and lateral gust wind speeds are introduced to simulate the random flight trajectory of roof sheathing. The Monte Carlo simulation results of the landing position of the roof sheathing in different gust sampling frequencies are compared with the wind tunnel results so as to determine the sampling frequency of the gust wind. The classical Runge-Kutta method used in the integration has four gradients in each time step; they are at the beginning, two middle, and ending

of the time step. Taking the time step as 0.05 s, five different gust sampling frequencies are examined in this paper, including

- sampling once at the beginning and middle of the time step with an interval of 0.15 s (0.75 s)
- sampling once at the beginning and middle of the time step with an interval of 0.10 s (0.05 s)
- sampling once at the beginning and middle of the time step with an interval of 0.05 s (0.025 s)
- sampling once at the beginning and two middle of the time step with an interval of 0.05 s (0.0167 s)
- sampling once at the beginning, two middle and ending of the time step with an interval of 0.05 s (0.0125 s)

Fig. 7 presents the comparison results of the Monte Carlo simulation and the wind tunnel test of the landing position of the roof sheathing at different gust sampling frequencies in the wind direction of 0°. The simulated landing positions of missiles are fairly concentrated when the sampling frequency is small. In the case of the large sampling frequency (0.0167 s and 0.0125 s), the landing positions of the roof sheathing are spread. Thus, the gust sampling frequency is determined to be sampling once at the beginning, two middle and ending of each time step (0.0125 s). The gust wind speed of each time step is randomly generated. In other words, the vertical and lateral gust wind speeds during the flight of the debris are not the actual gust wind speed in turbulent wind field.

3.4 Initial definition of extreme gust factor

According to Simiu and Scalan (1996), the gust factor of 0.10 is appropriate for the simulation of synoptic wind, whereas the gust factors of 0.25 and 1.0 are suggested for the simulation of hurricanes and tornadoes. These data are used as the reference value of the gust factor in the probabilistic trajectory model.

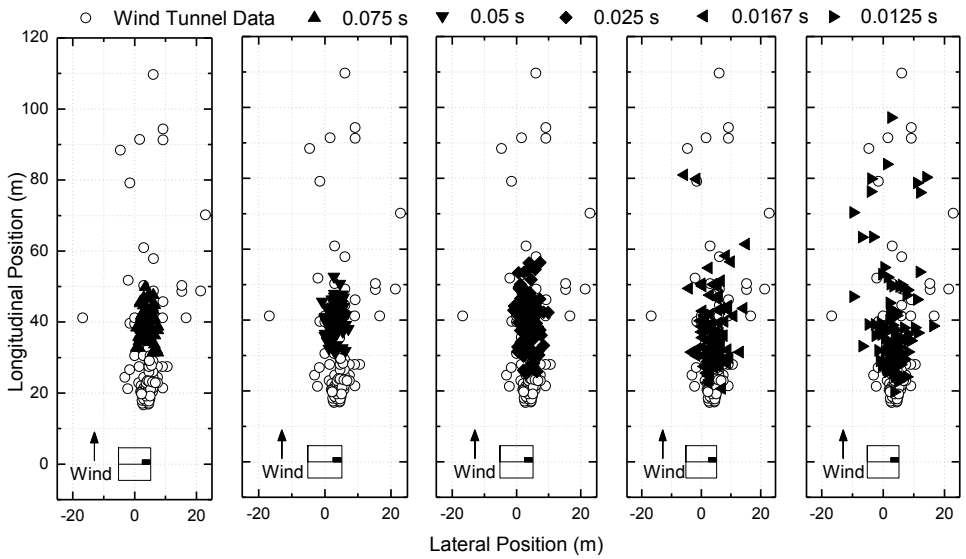

Fig. 7 Comparison results of the Monte Carlo simulation and the wind tunnel test of the landing position of the roof sheathing at different gust sampling frequencies in the wind direction of 0°

The definition of the extreme gust factor is to make the minimum SRSS errors of the simulated results of the landing position of the roof sheathing. The SRSS error is defined as

$$\varepsilon_{\text{total}} = \sqrt{\varepsilon_{\mu}^2 + \varepsilon_{\sigma}^2} \tag{23}$$

$$\mu = \frac{1}{n}\sum_{i=1}^{n} X_i \tag{24}$$

$$\sigma = \sqrt{\frac{1}{n-1}\sum_{i=1}^{n}(X_i - \mu)^2} \tag{25}$$

where μ and σ are the mean and standard deviation of the landing position of the roof sheathing, respectively.

The upper limit of the extreme vertical gust factor $\delta_{v\max}$ is determined to be 1.0 as the gust factor of 1.0 can simulate the tornado effect. By the trial calculation, it is found that the total error $\varepsilon_{\text{total}}$ decrease when the extreme lateral gust factor $\delta_{w\max}$ is trend to 1.0. Therefore, the upper limit of the extreme lateral gust factor is determined to be 1.5.

Fig. 8 shows the effect of $\delta_{v\max}$ and $\delta_{w\max}$ on the total error of the roof sheathing landing position, respectively. It is evident that the total error of the landing position of the roof sheathing first decrease, then increase with the increase in extreme gust factor. Moreover, the total error of the roof sheathing landing position become more sensitive to the extreme gust factor when the extreme gust factor is greater than 0.7. Therefore, the determination of the extreme gust factor should not only make the smallest total error but also make the extreme gust factor to be small. The initial values of the extreme vertical and lateral gust factors are shown in Table 2.

To further narrow the range of gust factor, the combined effect of the extreme vertical and lateral gust winds on the total error of the roof sheathing landing position was analyzed on the basis of the results in Table 2. As shown in Fig. 9, the total errors of the roof sheathing landing position for different combined extreme gust winds are obtained by the 100 Monte Carlo simulations of the flight trajectory of the roof sheathing. Fig. 9 shows the total error of the roof sheathing landing position for different combined extreme gust wind. It is evident that the areas with deeper color have smaller total error. The minimum total errors are less than 0.5 except for the case of the wind direction is 15°. According to the darker area in Fig. 9, the more accurate extreme gust factors are determined as shown in Table 3.

Table 2 The initial defined variation of the extreme vertical and lateral gust factor

Wind direction	Extreme vertical gust factor ($\delta_{v\max}$)	Extreme lateral gust factor ($\delta_{w\max}$)
0°	0.1–0.5	0.5–0.9
15°	0.3–0.7	0–0.4
30°	0.4–0.7	0.6–1.3
45°	0.3–0.8	0.6–1.3
60°	0.2–0.5	0.4–1.1

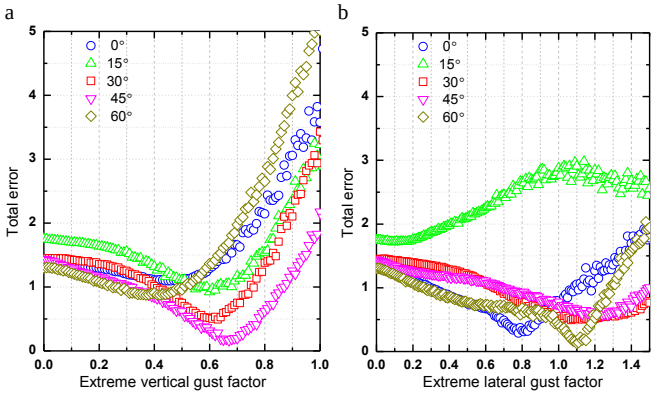

Fig. 8 Effect of (a) extreme vertical gust factor on the total error with the extreme lateral gust factor is 0 and (b) extreme lateral gust factor on the total error with the extreme vertical gust factor is 0 at each tested wind direction

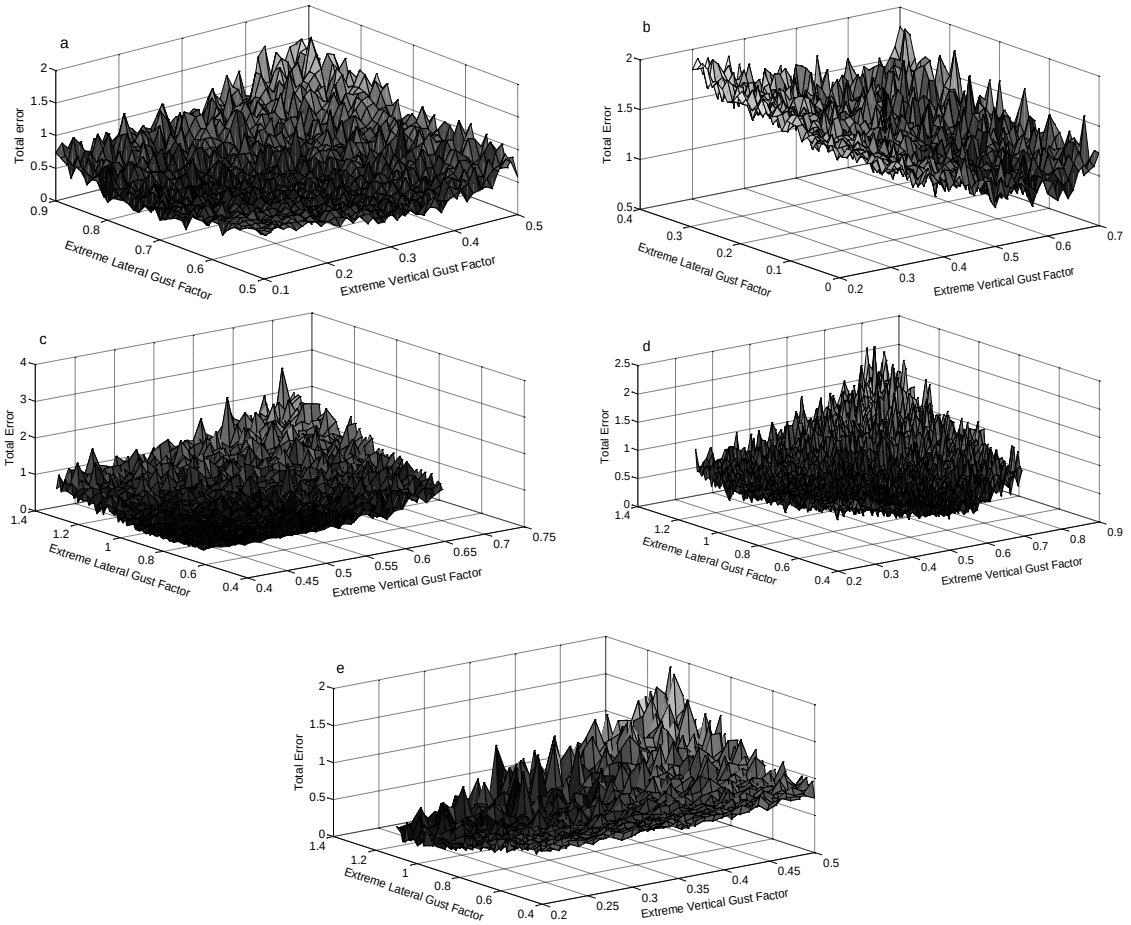

Fig. 9 Total error of the roof sheathing landing position vary with the extreme gust factor in the wind direction of (a) 0°, (b) 15°, (c) 30°, (d) 45° and (e) 60°

Table 3 The more accurate determined of the extreme vertical and lateral gust factor

Wind direction	Extreme vertical gust factor ($\delta_{v\max}$)	Extreme lateral gust factor ($\delta_{w\max}$)
0°	0.16–0.35	0.56–0.72
15°	0.46–0.66	0–0.17
30°	0.40–0.60	0.60–0.79
45°	0.42–0.67	0.60–0.81
60°	0.20–0.36	0.75–0.91

3.5 Number of simulations

The number of Monte-Carlo simulations is studied to determine the minimum number of simulations required for the results to become independent of the number of simulations. The standard deviation (STD) and coefficient of variation (COV) of the longitudinal landing position and lateral landing position is calculated and plotted against the number of simulations. The number of simulation increases firstly from 100 to 250, and then increases to 3000 at an interval of 250. The STD and COV of the landing position within a 5% error of its mean value are considered to be stabilized with the increase in the number of simulation. It can be seen from Fig. 10 that the STD and COV of the longitudinal landing position reaches equilibrium at a minimum of 1000 and 500 simulations, respectively. Furthermore, the STD and COV of the lateral landing position reaches equilibrium at a minimum of 1500 and 2000 simulations, respectively. Therefore, the minimum simulation number 2000 for the four landing position statistics reach equilibrium is selected to be the number of Monte Carlo simulation at the 0° wind direction. As shown in Table 4, the number of Monte Carlo simulation for other wind directions is also determined by this method.

3.6 Final determination of extreme gust factor

In order to simulate the flight trajectory of the roof sheathing more accurately, the extreme value of the gust factor is further analyzed to make the minimum total error of the landing position of the roof sheathing. In this part, the total error of the landing position of the roof sheathing is redefined as

Table 4 Number of Monte Carlo simulations

Wind direction	Number of simulation
0°	2000
15°	750
30°	1750
45°	1500
60°	2000

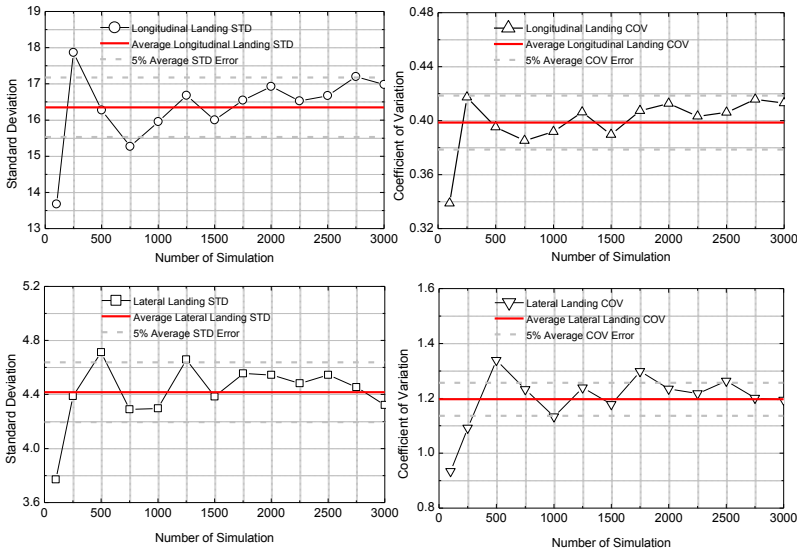

Fig. 10 Required number of simulations based on STD and COV of landing position in wind direction of 0°

$$\varepsilon_{\text{total}} = \sqrt{\varepsilon_{\mu}^2 + \varepsilon_{\sigma}^2 + \varepsilon_{s}^2 + \varepsilon_{k}^2} \tag{26}$$

$$s = \frac{\frac{1}{n}\sum_{i=1}^{n}(X_i - \mu)^3}{(\sqrt{\frac{1}{n}\sum_{i=1}^{n}(X_i - \mu)^2})^3} \tag{27}$$

$$k = \frac{\frac{1}{n}\sum_{i=1}^{n}(X_i - \mu)^4}{(\sqrt{\frac{1}{n}\sum_{i=1}^{n}(X_i - \mu)^2})^4} \tag{28}$$

where μ and σ are the mean and standard deviation of the landing position of the roof sheathing, respectively; s and k are the skewness and kurtosis of the landing position of the roof sheathing, respectively.

The numbers of the Monte Carlo simulation are increased from 100 to the numbers which have determined in *3.5*. On the base of the combination of extreme gust factor determined in *3.4*, the flight trajectory of the roof sheathing is simulated to obtain the combination of the extreme gust factor with the minimum total error of the roof sheathing landing position. Finally, the combinations of the extreme gust factor for different wind direction with minimum total error are determined as shown in Fig. 11.

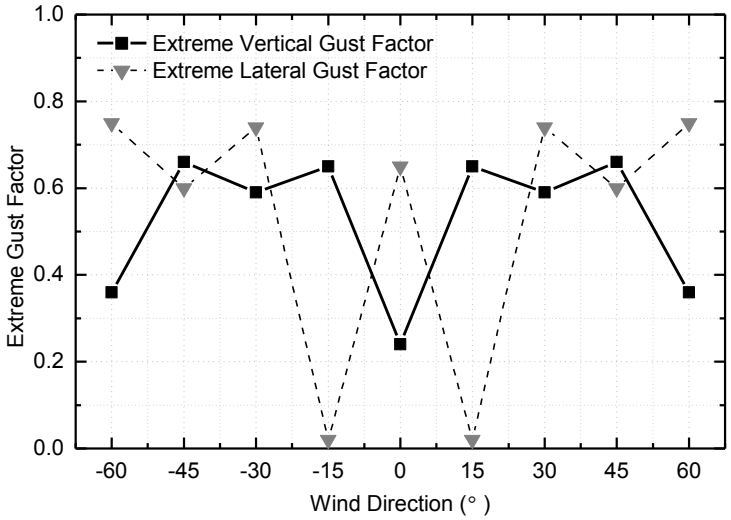

Fig. 11 The extreme gust factor in the probabilistic flight trajectory model

Kordi *et al.* (2010) observed that the roof sheathing landed back on the roof immediately after failure in the wind direction of 75° and 90°, therefore, it is assume that the extreme gust factor for the wind directions greater than 60° (or less than −60°) are the same as the extreme gust factor of the 60° (−60°) wind direction. The extreme gust factor for the wind direction between −60° and 60° is derived from linear interpolation.

4. Validation of the probabilistic trajectory model

To demonstrate the validity of the probabilistic trajectory model, the results simulated are compared with the scaled debris test data in Kordi *et al.* (2010). The comparison includes the impact position and impact velocity of the wind-borne debris. The comparison of the impact position consists of the distribution of the landing position, the relationship between initial wind speed and longitudinal landing location, and the distribution of the impact location at specific longitudinal position. The comparison of the impact velocity consists of the relationship of the dimensionless impact velocity with vertical impact position, the statistics and probability distribution of the dimensionless impact velocity at the landing time.

4.1 Impact position

For comparison, the 100 Monte Carlo simulations were conducted, which is the comparison to the number of debris flight trajectory test times in the wind tunnel test by Kordi *et al.* (2010). The simulation results and the wind tunnel test results of the flight trajectory are shown in Fig. 12. The simulated results of the impact position of roof sheathing agree well with the test results of Kordi *et al.* (2010), although the simulated results does not distinguish the flight mode (“3-D spinning”, “Auto-rotational”, and “Translational”) as recorded by Kordi *et al.* (2010).

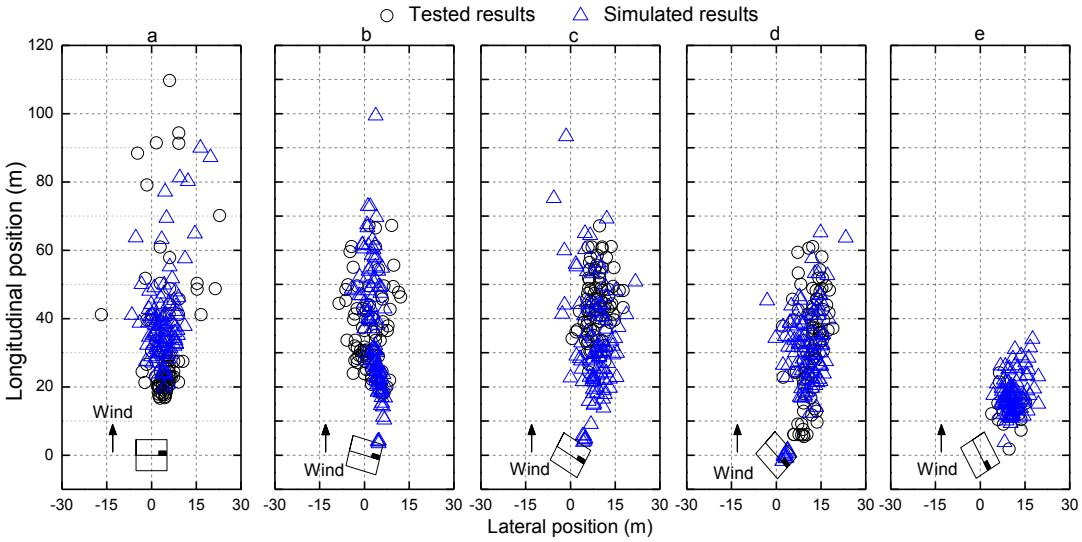

Fig. 12 Landing positions of 100 missiles in wind directions of (a) 0°, (b) 15°, (c) 30°, (d) 45°, and (e) 60°

Table 5 Comparison of simulated landing position data statistics with wind tunnel debris data

Wind direction	Tested results				Simulated results				Relative error
	X_{avg}	Z_{avg}	X_{σ}	Z_{σ}	X_{avg}	Z_{avg}	X_{σ}	Z_{σ}	$\varepsilon_{X_{avg}}$
0°	34	5	20	5	39	4	14	4	14%
15°	37	2	13	5	37	3	18	2	0%
30°	43	9	10	3	35	8	16	4	−19%
45°	32	12	15	4	30	10	14	5	−6%
60°	14	10	6	4	17	11	6	3	21%

Table 5 shows the comparison of the statistics (mean and standard deviation) of the roof sheathing impact position under different wind directions. In Table 5, X_{avg} and Z_{avg} are the mean values of the landing positions of the debris at the longitudinal and vertical directions, respectively. X_{σ} and Z_{σ} are the standard deviations of the landing positions of the debris at the longitudinal and vertical directions, respectively. ε_{Xavg} is the relative error of the tested and simulated results of the landing positions at longitudinal direction. Table 5 shows that the maximum relative error of the average longitudinal position is about 21%, occurring at the wind angle of 60°. Nevertheless, the simulated results of the roof sheathing impact position in the probabilistic flight trajectory model generally agree well with the wind tunnel test results.

Fig. 13 depicts the comparison results of the longitudinal debris impact position as a function of initial wind speed under different wind directions.

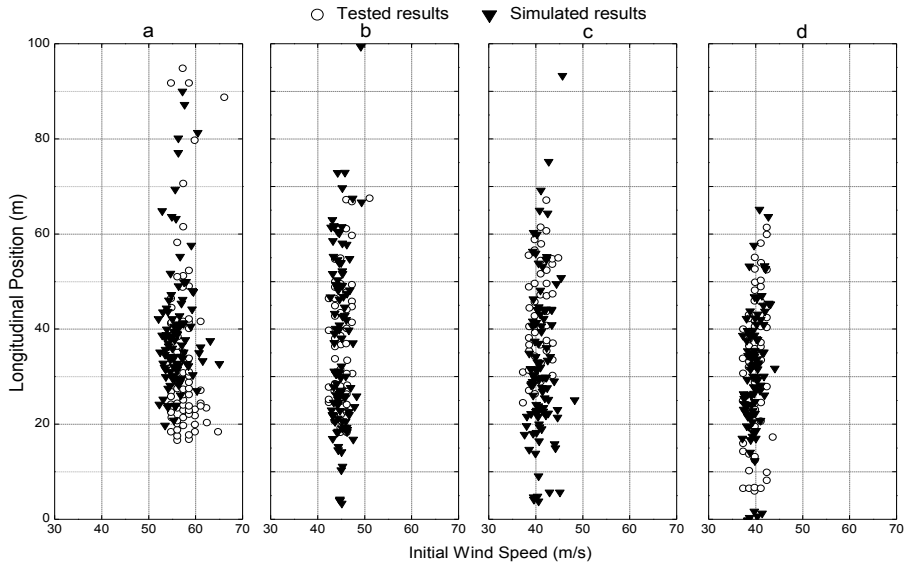

Fig. 13 Longitudinal debris landing position as a function of initial wind speed in wind directions of (a) 0°, (b) 15°, (c) 30°, and (d) 45°

The simulated results of the probabilistic flight trajectory model in the wind direction of 60° are not presented herein due to the lack of the pertinent wind tunnel data. Similarly, the simulation results are basically fit well with the wind tunnel test results. Furthermore, this plot confirms the findings in Kordi *et al*. (2010) that the variations in the mean wind velocity are not a dominant factor affecting the distribution of the landing position of the flying debris.

To verify the accuracy of the trajectory during the flight of the debris in the probabilistic model, the vertical impact positions of the roof sheathing at longitudinal locations of 20 m and 30 m in 15° and 30° wind directions are compared with the results in the wind tunnel test of Kordi *et al*. (2010), as shown in Fig. 14.

The data in Fig. 14 represent the impact positions of the debris on the surface of the building which is far away from the middle of the original building with longitudinal distances of 20 m and 30 m. For the lateral impact position, the simulated results of the probabilistic flight trajectory model coincide with the wind tunnel test results in the wind direction of 30°. However, the simulated results are slightly greater than the tested results in the wind direction of 15°. For the vertical impact position, the simulated results are in the range of 0 to 11 m and the tested results are in the range of 3 to 9 m at the longitudinal position of 20 m; the simulated results are in the range of 0 to 10 m and the tested results are in the range of 0 to 7 m at the longitudinal position of 30 m. The upper limit of the impact position of the simulated results is 2 to 3 m greater than that of the tested results. The simulated results trend toward safety, considering that the probabilistic flight trajectory model will be applied into the risk assessment of the impact damage of building envelopes.

Due to the lack of wind tunnel test data in wind direction of 0°, 45°, and 60°, Fig. 15 only shows the simulated results of the impact position for the longitudinal positions of 20 and 30 m.

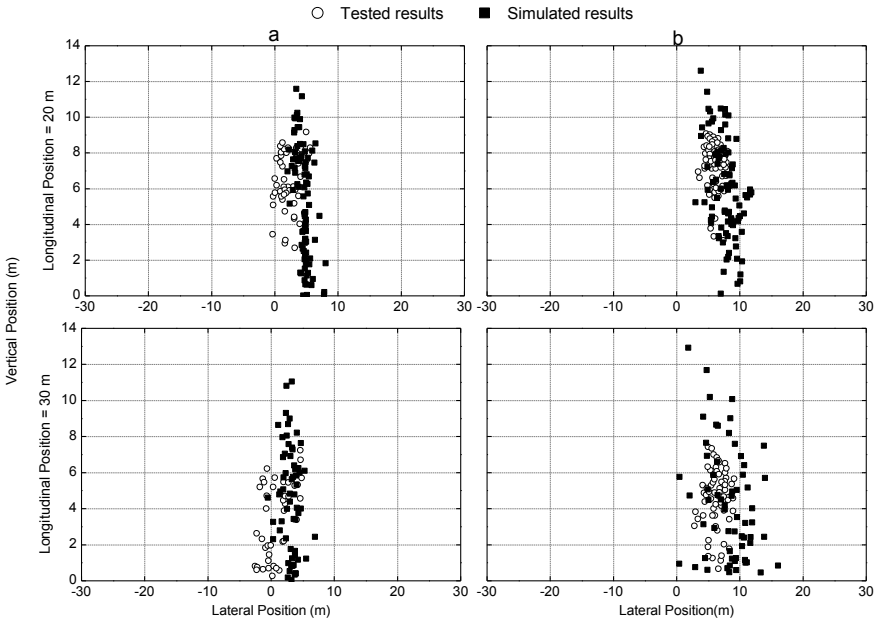

Fig. 14 Distributions of a roof sheathing in the vertical planes of longitudinal position = 20 m (top) and longitudinal position = 30 m (bottom) in the wind directions of (a) 15° and (b) 30°

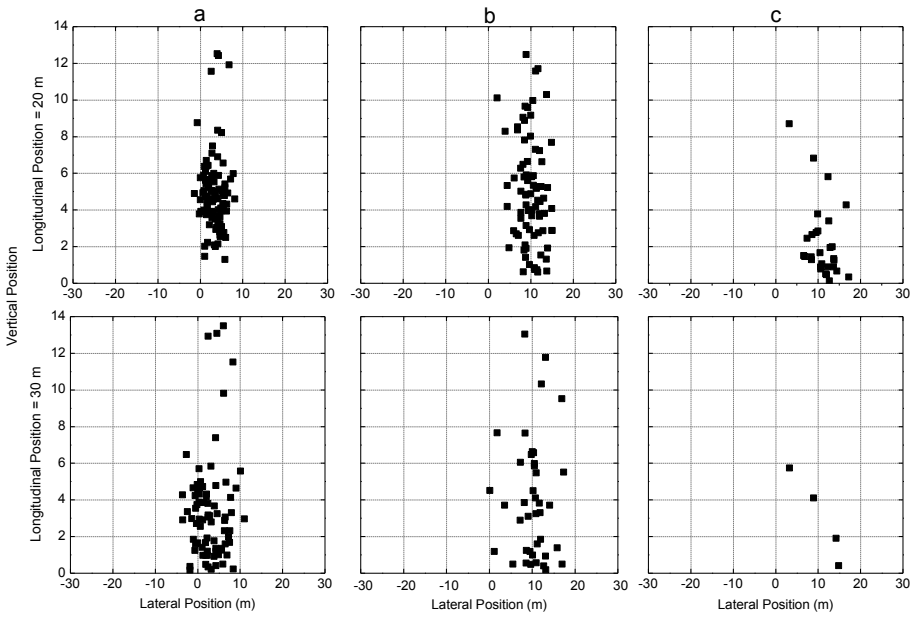

Fig. 15 Simulated positions of a roof sheathing in the vertical planes of longitudinal position = 20 m (top) and longitudinal position = 30 m (bottom) in the wind directions of (a) 0°, (b) 45°, and (c) 60°

4.2 Impact velocity

It has been well established that the impact velocity of the debris determines the momentum and kinetic energy of specific debris in the probabilistic flight trajectory model. The impact momentum and kinetic energy of the debris are of the main concern to estimate the failure of the building envelopes. Therefore, it is necessary to investigate the impact velocity of the debris in the probabilistic trajectory model. The total velocity (V_{mag}) of a missile is denoted as (Kordi *et al*. 2010)

$$V_{mag} = \sqrt{V_x^2 + V_y^2 + V_z^2} \tag{29}$$

where V_x is the longitudinal (horizontal) component, V_y is the vertical component, and V_z is the lateral component of the debris velocity.

According to Kordi *et al.* (2010), the longitudinal and total velocities of the debris are normalized by the equivalent full-scale 3-sec gust wind speed at the mean roof height

$$\bar{V}_x = \frac{V_x}{\hat{V}_H} \tag{30}$$

$$\bar{V}_{mag} = \frac{V_{mag}}{\hat{V}_H} \tag{31}$$

Fig. 16 illustrates the comparison results of the dimensionless longitudinal and total velocity as seen at a vertical slice of the roof sheathing at a longitudinal position of 20 m for the wind direction of 15° and 30°. Results show that the simulated results of the dimensionless velocity of the roof sheathing agree reasonably well with the wind tunnel test results, they are all in the range of 0.3–0.75. The dimensionless velocities of the roof sheathing in the range of 0.5–0.75 of the simulated results are more than the wind tunnel test results. For the 100 plates under investigate, there were about 60 plates flew to the longitudinal position of 20 m in the wind tunnel test of Kordi *et al.* (2010). However, there were about 90 plates flew to the longitudinal position of 20 m in the simulated results. It means that the simulated results of the flight velocity of the debris are tending to be slightly larger than the wind tunnel test results. The simulated results trend toward safety, considering the probabilistic flight trajectory model will be applied into the risk assessment of the impact damage of building envelopes.

In addition, the selection of the most appropriate extreme gust factor is to make the minimum error between the simulated and wind tunnel test results of the roof sheathing landing position. The flight velocity is not considered in the selection of the extreme gust factor, so the verification of the flight velocity can be appropriately relaxed.

Fig. 17 shows the simulated results of the dimensionless longitudinal and total impact velocity at a longitudinal position of 20 and 30 m for the 0°, 15°, 30°, 45° and 60° wind direction in the probabilistic trajectory model, as the wind tunnel test results are not available. We can see from Fig. 17 that the vertical impact position decreases obviously and the dimensionless total velocity of the roof sheathing increases significantly when the longitudinal positions increase from 20 m to 30 m for 0°, 15°, 30°, 45° and 60°wind direction as reported by Kordi *et al*. (2010).

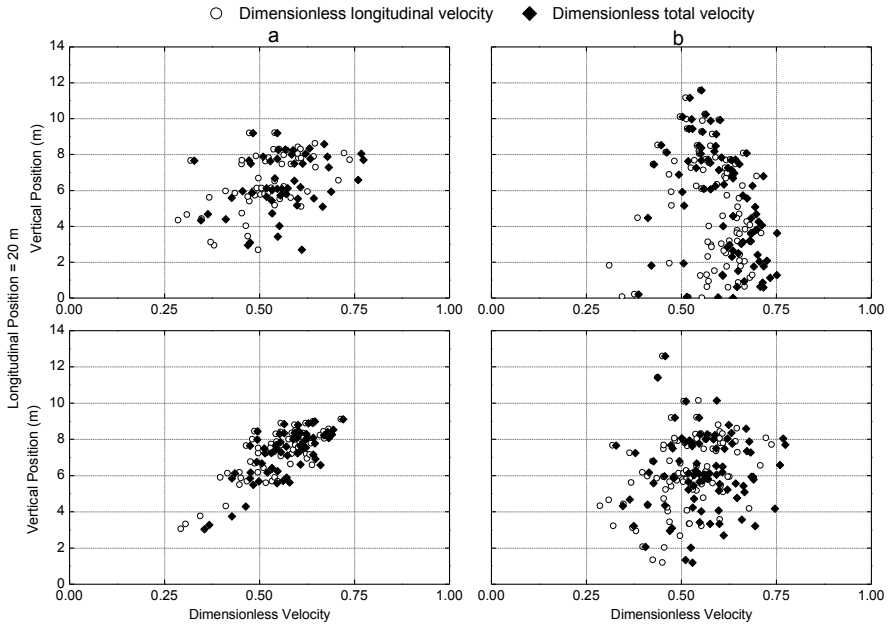

Fig. 16 (a) wind tunnel test and (b) probabilistic flight trajectory model results of the dimensionless panel velocities as a function of vertical position for wind direction of (top) 15° and (bottom) 30° at longitudinal position of 20 m

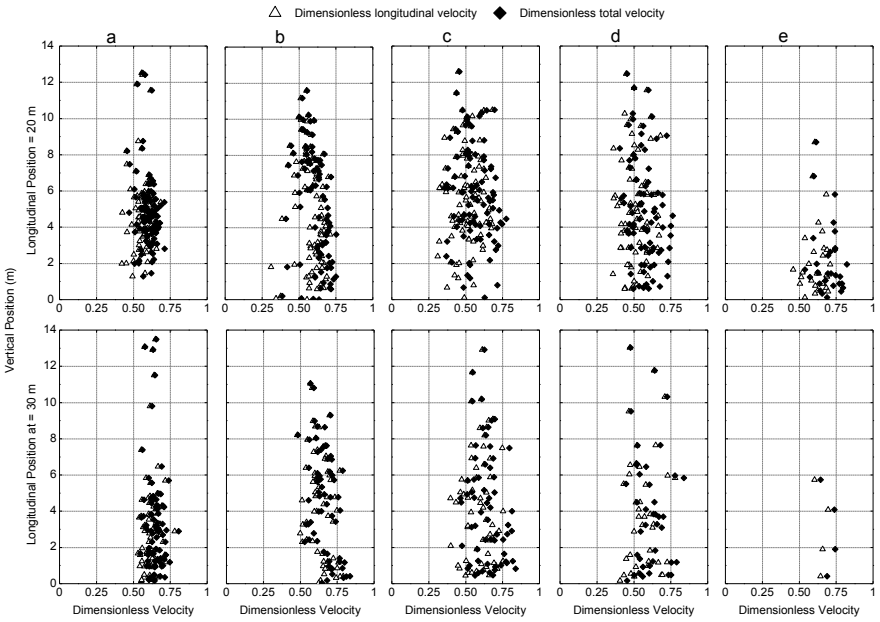

Fig. 17 Dimensionless debris velocities as a function of vertical position for wind direction of (a) 0°, (b) 15°, (c) 30°, (d) 45°, (e) 60° at (top) longitudinal position of 20 m and (bottom) longitudinal position of 30 m

Table 6 illustrates a comparison of the simulated and experimental dimensionless total velocity of the roof sheathing. The test results for the wind direction of 0° and 60° in the experimental of Kordi *et al.* (2010) are not available. The results for the wind direction of 15°, 30°, and 45° are compared in the follow. The simulated results of the probabilistic flight trajectory model agrees well with the test results of Kordi *et al.* (2010) except for the wind direction of 45°, the simulated results of the mean value of the dimensionless total velocity are greater than the experimental results of Kordi *et al.* (2010). For the standard deviation of the dimensionless total velocity, the simulated results are smaller than the experimental results. This is most likely due to the wind tunnel test speed observed by Kordi *et al.* (2010) may not necessarily be the same as the equivalent full-scale 3-sec failure gust speed at mean roof height. Since the probabilistic model does not account for the boundary conditions of the low-rise building, the assumption was made that the equivalent full-scale 3-sec failure gust speed measured at mean roof height reported by Kordi *et al.* (2010) is the wind speed experienced by the simulated plate. Therefore, there may be variability in the actual wind field experienced by the plate in the wind tunnel tests that the probabilistic model is unable to account for, which could explain the discrepancy between the variability of the physical and the simulated data.

Kordi *et al.* (2010) found that the dimensionless total velocity of the debris fit a lognormal distribution when the debris landing on the ground. For comparison, the dimensionless total velocities of the debris are researched by 100 simulations. Figs. 18 and 19 shows the probability density function and the corresponding probability distribution function of dimensionless total velocity at ground impact for the wind directions of 0°, 15°, 30°, 45°, and 60°, respectively. The probability density function and the corresponding probability distribution function are also compared with the fitted classic distribution such as lognormal distribution, type 1 extreme value distribution, and non-parametric estimation. It is evident that the distributions of the dimensionless total velocity of the debris at the landing position are fit with a lognormal distribution for all of the researched wind directions. Assuming a significance level of 0.05, the Kolmogorov-Smirnov one-sample test (KS) of the dimensionless total velocity confirmed that all cases are likely to come from a lognormal distribution.

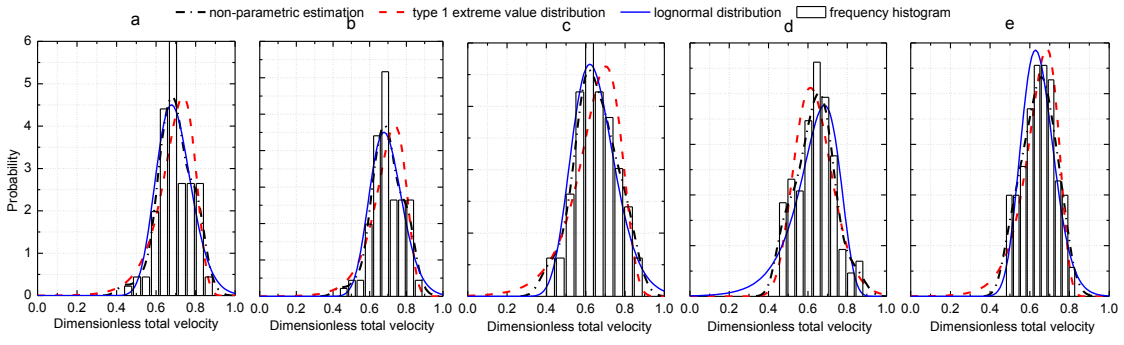

Fig. 18 Probability distribution of the dimensionless total velocity of a 1.2 m × 2.4 m × 12.7 mm roof sheathing at the landing position for wind directions of (a) 0°, (b) 15°, (c) 30°, (d) 45°, and (e) 60° simulated within the probabilistic debris trajectory model

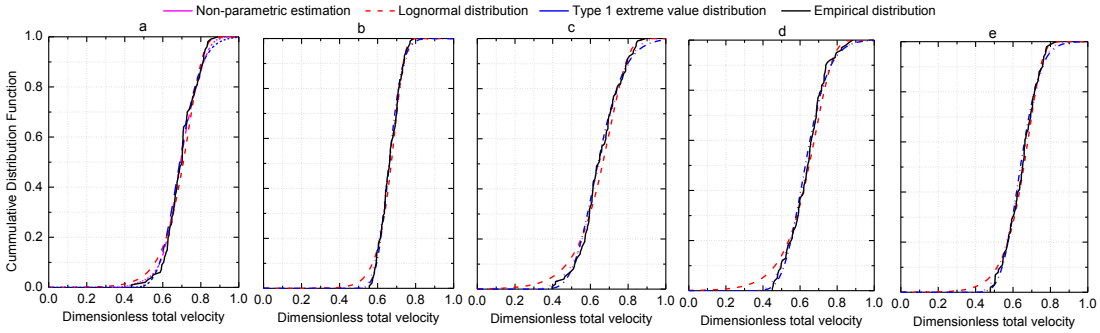

Fig. 19 Cumulative distribution of the dimensionless total velocity of a 1.2 m × 2.4 m × 12.7 mm roof sheathing at the landing position for wind directions of (a) 0°, (b) 15°, (c) 30°, (d) 45°, and (e) 60° simulated within the probabilistic debris trajectory model

Table 6 Comparison of the simulated and experimental dimensionless total velocity of the roof sheathing

Wind direction	Kordi *et al*. (2010)		Simulated results	
	$(\bar{V}_{mag})_{avg}$	$(\bar{V}_{mag})_{\sigma}$	$(\bar{V}_{mag})_{avg}$	$(\bar{V}_{mag})_{\sigma}$
0°			0.69	0.08
15°	0.73	0.21	0.67	0.12
30°	0.58	0.24	0.65	0.11
45°	0.43	0.20	0.64	0.12
60°			0.63	0.09

5. Conclusions

In this study, a deterministic 6 DoF debris trajectory model was employed in a combination of the randomly simulated vertical and lateral velocity components to predict the trajectory of the plate-type debris in a probabilistic manner. The proposed methodology accounted for the variations in the velocity field due to the aerodynamics of the building and the local roof velocities. A sensitivity analysis was conducted to determine the influence of the random variables, such as initial wind speed, time step, gust sampling frequency, number of simulation and extreme vertical and lateral gust factor, on the accuracy of the model.

The Monte Carlo simulation results of the 3-D probabilistic flight trajectory model are compared with wind tunnel test results and the following conclusions were obtained:

- The simulated results of the distribution and statistic of the impact location under different wind directions coincide with the wind tunnel test, and the relationship of the vertical impact position with the initial wind speed agrees well with the wind tunnel test results.
- At specific longitudinal location, the wind tunnel test results of the impact position of roof sheathing for the wind direction of 15° and 30° are under the curve line of the simulation

results. It means that the simulated result of the vertical impacted position is slightly larger than that of the experimental results. This simulation results trend toward safety, considering that the probabilistic flight trajectory model will be applied into the risk assessment of the impact damage of building envelopes.

- For the range of dimensionless impacted velocity of the roof sheathing, the simulated results are consistent with the experimental results under the wind direction of 15° and 30°. For the mean, standard deviation and coefficient of variation of the dimensionless impact velocity, there is a slight deviation between the simulated and tested results.

Acknowledgements

This project is jointly supported by the Ministry of Science and Technology of China (Grant No. SLDRCE14-B-09) and the National Natural Science Foundation (No. 51178352, 51378396 and 91215302), which are gratefully acknowledged.

References

Cline, M.B. and Pai, D.K. (2003), "Post-stabilization for rigid body simulation with contact and constraints". *Proceedings of the IEEE International Conference on Robotics and Automation*, *IEEE International Conference on.*

Fu, A.M., Huang, P. and Gu, M. (2013), "Numerical model of three-dimensional motion of plate-type wind-borne debris based on quaternions and its improvement in unsteady flow", *Appl.Mech. Mater.*, **405-408**, 2399-2408.

Grayson, J.M., Pang, W.C. and Schiff, S. (2012), "Three-dimensional probabilistic wind-borne debris trajectory model for building envelope impact risk assessment", *J. Wind Eng. Ind. Aerod.*, **102**, 22-35.

Kakimpa, B., Hargreaves, D.M. and Owen, J.S. (2012), "An investigation of plate-type windborne debris flight using coupled CFD–RBD models, Part II: Free and constrained flight", *J. Wind Eng. Ind. Aerod.*, **111**, 104-116.

Kareem, A. (1986), "Performance of cladding in Hurricane Alicia", *J. Struct. Eng.*, **112**(12), 2679-2693.

Kordi, B., Traczuk, G. and Kopp, G.A. (2010), "Effects of wind direction on the flight trajectories of roof sheathing panels under high winds", *Wind Struct.*, **13**(2), 145-167.

Kordi, B. and Kopp, G.A. (2011), "Effects of initial conditions on the flight of windborne plate debris", *J. Wind Eng. Ind. Aerod.*, **99**(5), 601-614.

Lee, B.E. (1988), "Engineering design for extreme winds in Hong Kong", *Hong Kong Eng.*, **16**(4), 15-23.

Lin N., Letchford, C. and Holmes, J. (2006), "Investigation of plate-type windborne debris. Part I: Experiments in wind tunnel and full scale", *J. Wind Eng. Ind. Aerod.*, **94**(2), 51-76.

Minor, J.E. (1994), "Windborne debris and the building envelope", *J. Wind Eng. Ind. Aerod.*, **53**, 207-227.

Moghim, F. and Caracoglia, L. (2012), "A numerical model for wind-borne compact debris trajectory estimation: Part 2 – Simulated vertical gust effects on trajectory and mass momentum", *Eng. Struct.*, **38**, 163-170.

National Association of Home Builders (NAHB) Research Center (2002), Wind-borne Debris Impact Resistance of Residential Glazing. U.S. Department of Housing and Urban Development, Office of Policy Development and Research, Cooperative Agreement H-21172CA, Washington, D.C., USA.

Noda, M. and Nagao, F. (2010), "Simulation of 6DOF motion of 3D flying debris", *Proceedings of the 5th International Symposium on Computational Wind Engineering (CWE2010)*, Chapel Hill, North Carolina, USA.

Richards, P.J., Williams, N., Laing, B. *et al*. (2008), "Numerical calculation of the three-dimensional motion of wind-borne debris", *J. Wind Eng. Ind. Aerod.*, **96**(10-11), 2188-2202.
Roache, P.J. (1997), "Quantification of uncertainty in computational fluid dynamics", *Annu. Review Fluid Mech.*, **29**(1), 123-160.
Simiu, E. and Scanlan, R.H. (1996), *Wind effects on structures*, New York, NY, USA: John Wiley and Sons.
Tachikawa, M. (1988), "A method for estimating the distribution range of trajectories of wind-borne missiles", *J. Wind Eng. Ind. Aerod.*, **29**, 175-184.
Visscher, B.T. and Kopp, G.A. (2007), "Trajectories of roof sheathing panels under high winds", *J. Wind Eng. Ind. Aerod.*, **95**, 697-713.
Warga, J. (1976), *Derivate containers, inverse functions, and controllability*, Calculus of Variations and Control Theory, DL Russell, Ed., Academic Press, New York, 13-46.
Wills, J.A.B., Lee, B.E. and Wyatt, T.A. (2002), "A model of windborne debris damage", *J. Wind Eng. Ind. Aerod.*, **90**, 555-565.

CC